

Combined Visualization of Wall Thickness and Wall Shear Stress for the Evaluation of Aneurysms

Sylvia Glaßer, Kai Lawonn, Thomas Hoffmann, Martin Skalej, Bernhard Preim

Abstract—For an individual rupture risk assessment of aneurysms, the aneurysm's wall morphology and hemodynamics provide valuable information. Hemodynamic information is usually extracted via computational fluid dynamic (CFD) simulation on a previously extracted 3D aneurysm surface mesh or directly measured with 4D phase-contrast magnetic resonance imaging. In contrast, a non-invasive imaging technique that depicts the aneurysm wall in vivo is still not available. Our approach comprises an experiment, where intravascular ultrasound (IVUS) is employed to probe a dissected saccular aneurysm phantom, which we modeled from a porcine kidney artery. Then, we extracted a 3D surface mesh to gain the vessel wall thickness and hemodynamic information from a CFD simulation. Building on this, we developed a framework that depicts the inner and outer aneurysm wall with dedicated information about local thickness via distance ribbons. For both walls, a shading is adapted such that the inner wall as well as its distance to the outer wall is always perceivable. The exploration of the wall is further improved by combining it with hemodynamic information from the CFD simulation. Hence, the visual analysis comprises a brushing and linking concept for individual highlighting of pathologic areas. Also, a surface clustering is integrated to provide an automatic division of different aneurysm parts combined with a risk score depending on wall thickness and hemodynamic information. In general, our approach can be employed for vessel visualization purposes where an inner and outer wall has to be adequately represented.

Index Terms—Aneurysm, IVUS, Wall Thickness, Wall Shear Stress, Brushing and Linking, Focus + Context

1 INTRODUCTION

The understanding of vascular diseases, such as coronary heart disease and aneurysms, benefits from an expressive visualization of the vessel wall comprising the inner border (between lumen and vessel wall) and the outer border (between vessel wall and surrounding tissue) – which we will refer to as inner and outer wall. Vascular diseases are not only characterized by deposits that lead to vessel narrowing but also by vascular wall remodeling. While widespread imaging modalities only represent the inner vessel wall, usually enhanced with a contrast agent, recent developments in imaging technology enable the detection of the inner and the outer wall. An expressive visualization of the inner and outer vessel wall is a special instance of an embedded surface visualization, where the local distances between two flexible tube-like structures should be conveyed. The simple semi-transparent rendering of the outer shape is not ideal to convey its shape and its spatial relation to inner objects (see e.g., [21]). In this paper, we present a new technique for this problem, inspired by but not limited to the requirements of the diagnosis of the vascular diseases.

As a case study we consider cerebral aneurysms – pathologic dilatations of the neurovascular vessel wall. Inherent to aneurysms is the risk of rupture, which may cause a subarachnoid hemorrhage. The treatment options comprise endovascular intervention and neurosurgical clipping with a high rate of complications in relation to the rupture rate of asymptomatic aneurysms. Thus, patients with asymptomatic cerebral aneurysms would often benefit from a wait and see strategy. However, they mostly chose interventional treatment due to the psychological burden of knowing the rupture risk which underpins the strong need for patient-specific rupture analysis.

Important for rupture risk assessment are the hemodynamic information and the vessel wall morphology. The hemodynamic behavior,

e.g., the complexity of flow patterns extracted from computational fluid dynamics (CFD), reportedly influences the rupture risk [8]. Still, a ground truth is not available since CFD may be too imprecise. Furthermore, the internal blood flow depends on the wall morphology. Additionally, an increased rupture rate is reported for super-thin aneurysm walls as well as heterogeneous walls based on analyses during neurosurgical clipping [15].

In summary, for an improved patient-specific rupture risk assessment and thus improved treatment decision (e.g., endovascular therapy, surgical clipping or no therapy at all), hemodynamic and wall morphology information are needed. Thus, we investigate how the vessel walls and the flow information based on CFD simulations may be displayed simultaneously. We focus on the wall thickness WT and the wall shear stress WSS . In particular, we are interested in highlighting parts of the vessel wall where the WT and the simulated WSS values are in a certain range. Therefore, a comprehensive 3D visualization will be presented in this paper. Our contributions are summarized as follows:

- A novel simultaneous 3D visualization of the inner and outer vessel wall. The WT is conveyed via distance ribbons and adapted, view-dependent GPU shading techniques.
- Hemodynamic information (and a combination with WT) is provided via color-coding of the inner aneurysm wall surface.
- The visual exploration of the aneurysm model comprises brushing and linking (in the parameter space spanned by WT and WSS) as well as a surface clustering to provide surface clusters with similar parameter values on the inner vessel wall.
- Finally, a qualitative evaluation with domain experts indicates the value of the visualization and the strong need for wall morphology information.

2 RELATED WORK

In this section, we discuss related work for the visual exploration of cardiovascular diseases and cerebral aneurysms with focus on the simultaneous depiction of outer and inner vessel wall. The related work for cerebral aneurysms is extendable to general aneurysms.

Visual exploration of cardiovascular diseases. The simultaneous visualization of inner and outer vessel wall plays an important role for

- Sylvia Glaßer, Kai Lawonn and Bernhard Preim are with the Department for Simulation and Graphics, at the Otto-von-Guericke University of Magdeburg, Germany. E-mail: {glasser,lawonn,preim}@ovgu.de.
- Thomas Hoffmann and Martin Skalej are with the Neuroradiology Department of the University hospital of Magdeburg, Germany. E-mail: {t.hoffmann,martin.skalej}@med.ovgu.de.

Manuscript received 31 Mar. 2014; accepted 1 Aug. 2014. Date of publication 11 Aug. 2014; date of current version 9 Nov. 2014.

For information on obtaining reprints of this article, please send e-mail to: tvcg@computer.org.

Digital Object Identifier 10.1109/TVCG.2014.2346406

3 MEDICAL BACKGROUND

Aneurysms are dilations of blood vessels that bear the risk of rupture causing hemorrhages. Mostly, they occur in the intracranial vessel system as well as in the thoracic and abdominal aorta. With increasing size, treatment is carried out to prevent the rupture. We explain the challenges of treatment decision for the specific example of cerebral aneurysms.

Patients with asymptomatic intracranial aneurysms often chose an interventional treatment over a conservative monitoring due to psychological factors. Hence, advanced and patient-specific rupture risk analyses could improve the decision making. Furthermore, the therapy of unruptured aneurysms may lead to complications as well. The rupture rates of asymptomatic intracranial aneurysms are reportedly equalled or exceeded by the mortality rate associated with treatment [43]. The most important risk factors are the type (asymptomatic or symptomatic), age, gender, size and location [42]. Although these risk factors are already integrated in clinical treatment decision making, the interaction of these factors is still largely unknown. To evaluate the patient-specific rupture risk, biomedical researchers investigate further factors and their influence on aneurysm initiation and growth.

The blood flow information plays an increasing role for diagnosis and treatment of cardiovascular diseases [28]. Recent studies reported a correlation between certain hemodynamic information (e.g., concentrated inflow jets, small impingement regions, complex or unstable flow patterns) and prior aneurysm rupture [9]. The hemodynamic information is derived from CFD simulation on a previously extracted 3D aneurysm surface mesh [8] or directly measured with 4D phase contrast magnetic resonance imaging [28]. Hence, the *WSS* describes the friction of the intravascular blood flow along the inner vessel wall and arises from the blood flow force vector component parallel to the cross section. The *WSS* has a strong influence on vessel wall remodeling. Increased *WSS* was correlated with prior aneurysm rupture [10] due to its destructive influence on the vessel wall's remodeling. However, also microbiological factors have to be considered since oscillating (including lower) *WSS* values may cause this effect [12]. Hence, no ground truth has been established yet.

Neurosurgeons report a relationship between wall thickness and risk of rupture. This relationship is poorly documented since no in vivo technique is available to measure aneurysm wall thickness. Studies based on analyses during neurosurgical clipping report increased rupture rates for super-thin as well as heterogeneous aneurysm walls [15]. Histological and intraoperative observational studies identified an aneurysm wall as a highly variable region (with a thickness from 16 to 400 μm) that contains areas of thick, intermediate and super-thin translucent tissue [24].

In summary, for an individual rupture risk assessment, the treatment decision would strongly benefit from the integration from hemodynamic and vessel wall information. This can be extended to aneurysms in general, e.g., rupture of abdominal aortic aneurysms is associated with thin vessel walls [32] and thoracal aortic aneurysms are characterized by pathological changes in the aorta's media wall [37]. We provide a framework that includes a pipeline that assesses the aneurysm wall with IVUS. This is motivated by cardiovascular diseases where IVUS provides valuable information about the coronary wall morphology [39]. Since the intravascular imaging of cerebral vessel wall is an active research area, we focus on the application scenario of cerebral aneurysms.

4 IMAGE ACQUISITION AND PREPROCESSING

Our approach can be divided into a preprocessing and a rendering step, see Figure 1. In this section, the preprocessing is explained, including the dissection and probing of the saccular artery aneurysm. Next, the extraction of the surface mesh, the *WT* and the hemodynamic information is explained. Finally, we describe the surface clustering approach. Based on the extracted 3D model, a comprehensive 3D visualization was developed, which will be explained in more detail in Section 5. The visualization allows for assessment of the vessel's *WT* as well as the simultaneous evaluation of thickness and hemodynamic information like *WSS*.

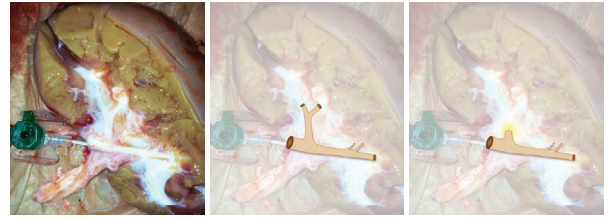


Fig. 2. Preparation of the saccular aneurysm. Left, the porcine kidney is shown. In the middle, an artery with a bifurcation is dissected. Right, the artery branch was shortened of ca. 4 mm and closed yielding the aneurysm.

4.1 Dissection and Image Acquisition of the Saccular Artery Aneurysm Dataset

To overcome the missing in vivo imaging technique to depict the vessel wall, we dissected an artificial aneurysm from a porcine kidney artery of a dead pig, see Figure 2. Dissection was carried out within a clinical environment. We selected an artery with a bifurcation and shortened and closed the smaller branch. The preparation exhibits similar attributes like cerebral arteries, but can be probed with IVUS.

The dissected aneurysm was put on tubes and integrated into an artificial blood flow circle. Hence, no pumping was simulated. Next, IVUS was probed along the parent vessel with an IVUS system (Volcano Corp., San Diego, USA). During image acquisition, a saline solution was injected, see Figure 3. A catheter was inserted into the vessel and pulled back along the parent vessel with constant velocity yielding a stack of 2D grayscale images that depict the vessel cross sections. The typical image parameters are: 512×512 pixels, IVUS diameter 20 mm and a pullback speed of 1 mm/s.

4.2 Extraction of the 3D Surface Mesh

Vessel wall detection algorithms as well as surface net generation approaches were adapted to the resulting IVUS dataset such that a 3D aneurysm model was created. For this purpose, a software prototype was developed with *MATLAB*. Our postprocessing was inspired by [18], where the inner coronary artery wall was segmented based on the following steps:

1. Preprocessing of the IVUS image.
2. Initial segmentation of the inner vessel wall.
3. Iterative adaption of an active contour to the initial inner wall segmentation.
4. Extraction of the outer wall by repeating steps 2 and 3.
5. *Optionally: One-click user interaction for additional parts.*
6. Combining inner and outer wall into a 3D surface mesh.

1. Preprocessing of the IVUS image. Due to the image acquisition, the catheter reflection is mapped on each vessel's cross section, see Figure 4(a). This reflection is masked out, and the boundary region around the circular mask is smoothed via Gaussian filtering to prevent

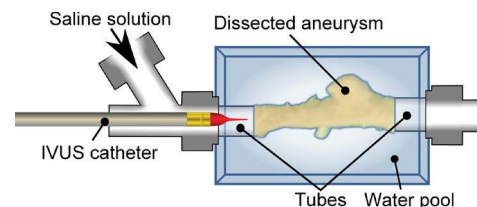


Fig. 3. Probing of the aneurysm. During IVUS data acquisition, a saline solution was continuously injected (without pumping).

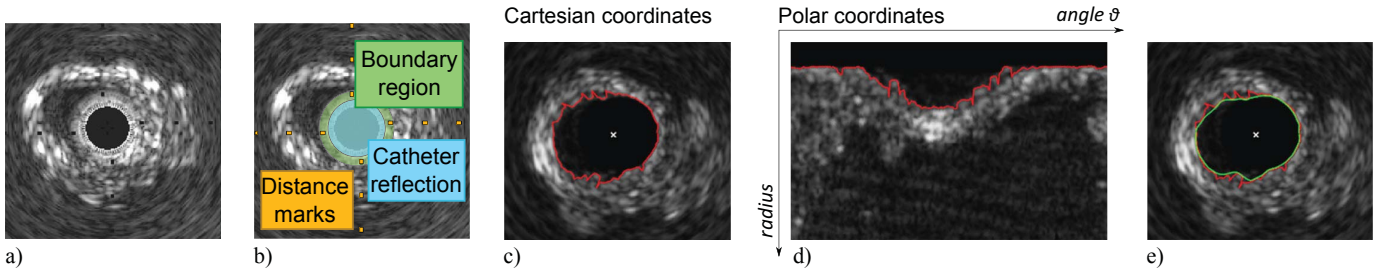


Fig. 4. Preprocessing of the IVUS image data. In (a) and (b), the original dataset is depicted. The initial contour (red) extraction can be seen in (c) and (d). The result of the iterative snake (green) adaption is illustrated in (e).

sharp edges in the boundary region (see Fig. 4(b)). The distance marks are removed by replacing these predefined intensities by the mean values of their surrounding voxels. Due to the ultrasound inherent properties like low dynamic range, (blood) speckle and the low signal-to-noise ratio [33], the whole image data is again smoothed with Gaussian filtering to reduce the high frequency noise. We employed a $2D\ 3 \times 3$ kernel and a σ -value of 2.0, similar to the approach presented in [18]. In [33], more complex preprocessing methods and combinations for 3D ultrasound data are described, comprising speckle removal methods for contour smoothing, median filters for gap closing in addition to the Gaussian filtering for noise reduction. In our case, the final segmentation result was sufficient based on the described filtering.

2. Initial segmentation of the inner vessel wall. For the initial segmentation, a transformation into polar coordinates was carried out. Thus, the vessel walls can be detected as horizontal structures, see Figure 4(c)-(d). As proposed in [18], a binary threshold segmentation yields line segments of the initial contour. Hence, for each angle ϑ the voxel with smallest radius that exhibits a signal intensity larger than the threshold is selected yielding the initial inner vessel wall.

3. Iterative adaption of an active contour. In contrast to [18] where (based on the initial contour) ellipses were fitted to the IVUS images, we employed cubic B-splines to approximate the vessel wall. Hence, an aneurysm may exhibit an arbitrary morphology including varying cross sections. We iteratively adapted an active contour, also called *snake* [25]. The active contour segmentation is an established method in cardiology image analysis [39]. The snake is a parametrized curve $v(s)$. It is influenced by image forces that pull it towards features. The actual parametric position of a snake can be represented as $v(s) = (x(s), y(s))^T$ with its energy functional:

$$E_{snake}(v(s)) = \int_0^1 E_{int}(v(s)) + E_{ext}(v(s)) ds. \quad (1)$$

The term $E_{int}(v(s))$ refers to the internal spline energy, i.e., a first-order term and a second-order term, controlled by $\alpha(s)$ and $\beta(s)$:

$$E_{int}(v(s)) = \alpha(s) \left| \frac{dv}{ds} \right|^2 + \beta(s) \left| \frac{d^2v}{ds^2} \right|^2. \quad (2)$$

$E_{ext}(v(s))$ refers to the external energy:

$$E_{ext}(v(s)) = w_1 f(x, y) - w_2 |\nabla(G_\sigma(x, y) * f(x, y))|^2, \quad (3)$$

where w_1 and w_2 are weights which represent the influence of the gray value $f(x, y)$ and the gradient $\nabla(G)$. The gray values are assumed to be normally distributed with the standard deviation σ . The initial snake was created as a parametrized spline based on the initial line (back-projected to Cartesian coordinates and connected to ensure a closed curve). We empirically determined the following weights: $\alpha = 0.3$, $\beta = 3.0$, $w_1 = 1$, $w_2 = 0.8$. Hence, small changes of these parameters hardly influenced the segmentation result. The iterative process terminates after no significant improvements were achieved. Since the extraction of inner and outer wall was carried out during preprocessing, the time consumption was not of interest. The resulting snake is depicted in Figure 4(e).

4. Extraction of the outer wall. The outer vessel wall was extracted in the same way. That means, the voxels with largest radius (see Fig. 4(d)) that exhibit a signal intensity larger than the threshold were selected and the process as described above is performed.

5. One-click user interaction for additional parts. With this optional step, the segmentation result can be improved. For the special case of overlapping structures, i.e., aneurysm parts that cannot be characterized by a single spline in an IVUS cross-sectional view (see Fig. 5(b)), we include a one-click user interaction. Hence, the user clicks into the lumen of the additional aneurysm part to define a seeding point. Then, a 2D region growing algorithm is applied for this slice which is feasible due to the small area of such additional parts. A second snake is initialized based on the border of the extracted region and fitted.

6. Combining inner and outer wall into a 3D surface mesh. We employ the parametrized splines to create two 3D surface meshes for the inner and outer wall. That means, for two subsequent contours, the discrete positions (we chose $n = 128$) are extracted from the splines and joined with triangles, see Figure 5(a). If a slice of the IVUS image holds two contours (due to the optional manual addition of overlapping aneurysm parts), the triangulation is adapted to this branching. Therefore, we resample and split the contour of the previous slice from n points to $2n-2$. The split yields two new contours with n points since the contours share an edge. This edge is automatically determined by minimizing the distances between the contours of the subsequent slices. The triangulation is then carried out individually for each of the slice contours (see Fig. 5(c)). If the current slice holds one contour and the previous slice holds two contours, i.e., the overlapping part stopped, the contour with larger distance is triangulated, i.e., filled with triangles itself. Our described problem is a special case of the branching problem, see [29] for more information. Due to the variable spline parametrization, the triangulation could be easily adapted.

4.3 Extraction of the Wall Thickness and the Hemodynamic Information

Due to their importance for rupture risk assessment, we focus on the two parameters wall thickness (WT) and wall shear stress (WSS). The extraction of these parameters is described in the following.

As a preprocessing step, the initial 3D surface meshes comprising inner and outer wall are optimized with respect to mesh quality. Therefore, an advancing front approach is applied that employs edge collapses and edge flips [35]. Next, an unstructured volume mesh is created based upon the inner wall mesh. Afterwards, the hemodynamic information was gained via CFD simulation employing the unstructured volume mesh. The mesh optimization results in an improved volume mesh and ensures convergence of the simulation. Hence, the blood flow was modeled as incompressible Newtonian fluid with rigid walls [8]. For the presented framework, we focus on the WSS. We extracted the parameter wall thickness WT for each point on the optimized inner surface mesh as minimum possible distance to the points of the outer surface mesh.

4.4 Surface Clustering

To support the subsequent visual exploration and analysis of the extracted aneurysm, we clustered all points of the inner surface mesh.

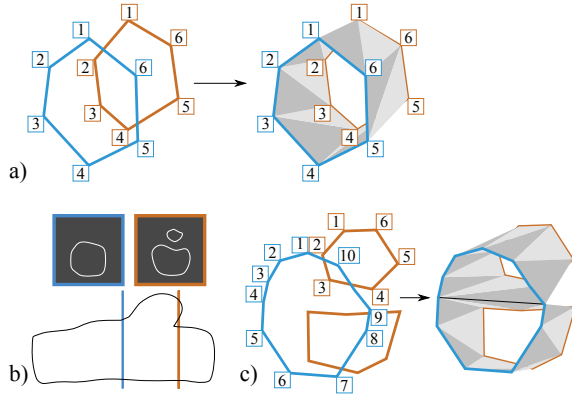


Fig. 5. Triangulation of two segmented contours from two subsequent image slices (a). In case of additional contours due to overlapping structures (b), the first spline is resampled with $2n - 2$ points and triangulation is carried out as illustrated in (c).

We adapted the bottom-up hierarchical clustering *region merging* where only neighbored clusters could be merged into a new cluster. Cluster c_i and cluster c_j are neighbored, if c_i contains a point that is connected to a point of cluster c_j via an edge on the 3D surface mesh. Initially, each point forms a single cluster. Then, the two neighbored clusters with the overall best similarity are iteratively merged into a new cluster. If the best similarity exceeds a certain threshold ε , the region merging terminates. We define the *risk* vector \vec{r}_i for a vertex i :

$$\vec{r}_i = \begin{pmatrix} WSS_i \\ 1 - WT_i \end{pmatrix} \quad (4)$$

For the extraction of \vec{r} , both parameter spaces are normalized to the interval $[0,1]$. Thus, points on the surface with low WT and high WSS yield larger values for $\|\vec{r}\|$ than points with a local thick wall and low WSS values. The definition of the \vec{r} was approved by the medical experts with whom we discussed and evaluated the presented work. The similarity sim_{ij} between clusters c_i and c_j is extracted as

$$sim_{ij} = \|\vec{R}_i - \vec{R}_j\|, \quad (5)$$

where \vec{R}_i is defined as the average value of WSS and $(1 - WT)$ for a cluster c_i , precisely:

$$\vec{R}_i = \frac{\int_{c_i} \vec{r} dx}{\int_{c_i} dx}. \quad (6)$$

To support various divisions of the surface into clusters, we precompute the clustering result for $\varepsilon \in \{0.05, 0.1, 0.15, 0.2, 0.25\}$. During clustering, all regions are stored in a region adjacency graph.

5 VISUALIZATION FRAMEWORK

In this section, we describe the different visualization and exploration techniques of our framework. As depicted in Figure 1, the rendering step comprises the shading of the outer wall (Sect. 5.1) and the color-coding of the inner wall's surface mesh (Sect. 5.2). Hence, the visualization is adapted to avoid occlusions. The third part describes the exploration of the 3D scene in more detail (Sect. 5.3).

5.1 Visualization of the Outer Wall

The outer wall is displayed with a ghosted-view approach based on the Fresnel shading according to [17]. They employed a Fresnel-reflection model [34] and mapped this to the aneurysm's wall opacity. The suitability of this technique for that purpose was validated in a perceptual user study [3]. The opacity o is determined by $o = 1 - |\langle \mathbf{v}, \mathbf{n} \rangle|^r$, where $\langle \cdot, \cdot \rangle$ denotes the dot product, \mathbf{n} is the surface normal, \mathbf{v} is the view vector, and $r \geq 0$ is the edge fall-off parameter. As a standard setting we use $r = 1.5$. With smaller values (e.g., $r = 1$), the salient regions

on the outer wall would disappear. Higher values would interfere with the visibility of the inner wall. As this information is only important for gaining an impression of the thickness, a white color is used. This avoids a distraction of mixed colors when focusing on the inner wall. Hence, the color of the outer wall is determined by $\text{color}_{Outer} = \mathbf{I} \cdot o$, where $\mathbf{I} = (1 \ 1 \ 1 \ 1)$ represents the RGBA values. If the user is interested in certain areas of the inner wall and zooms to this area, the outer wall may disturb the systematic investigation. To prevent this effect, a fade-out is implemented. The opacity of the outer wall fragments depends on the distance to the view point. Thus, the final color is determined by:

$$\text{color}_{Outer} = \mathbf{I} \cdot o \cdot \text{dist}.$$

The distance dist is measured in camera space. Therefore, a slight fading effect guarantees that the outer wall disappears when the view point is close, see Figure 6.

5.2 Visualization of the Inner Wall

For the inner wall visualization, we employ a color-coding with respect to a selected parameter (WT , WSS or $\|\vec{r}\|$). We chose a 1D white to brown colormap, see also Figure 6. The parameter spaces are scaled into the interval $[0,1]$ to employ the color map for the inner surface mesh points. Beyond the direct representation of each point's parameter values, we computed a surface clustering to provide surface clusters (recall Sect. 4.4). For color-coding, the surface integral S for each cluster c_i of the riskiness $\|\vec{r}\|$ is determined:

$$S_i = \frac{\int_{c_i} \|\vec{r}\| dx}{\int_{c_i} dx}.$$

As the value of S_i lies in the interval $[0,1]$, we again assign the 1D color map from $[0,1]$ to every cluster c_i (as shown in Fig. 6). Thus, every fragment of the inner wall is colored according to its associated cluster region. For a better differentiation of adjoined cluster regions, a border is displayed additionally. As the underlying vessel structure is a triangulated surface mesh, three cases may occur (see Fig. 7). First, all triangle points belong to the same cluster and the triangle is rendered with the assigned cluster's color. In the second case, two of three points in a triangle share the same surface cluster, and in the third case all points are associated to different clusters. For the second case, the border is created by connecting the midpoints of the lines that are incident to the point of the divergent cluster. For the last case, the triangle's centroid is connected to the midpoint of the edges.

5.3 Data Analysis

Our framework contains a 3D view where the representation of the outer wall serves as context object and the inner wall with its surface clusters is our focus object. Based on in-depth discussions with our clinical experts, we provide additional techniques to explore the 3D scene. First, the estimation of WT is supported by adaption of distance ribbons, which will be explained in more detail. Second, we developed the global and local scatterplot, including a brushing and linking facility, for the interactive exploration of the data. Furthermore, the

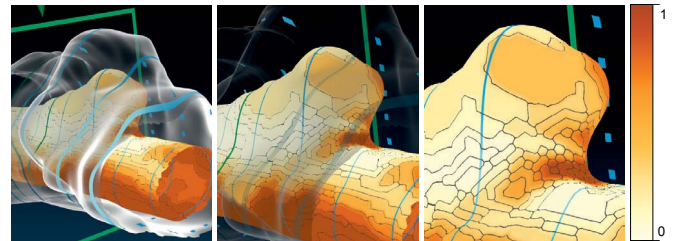


Fig. 6. Illustration of the fading effect of the outer vessel wall visualization. From left to right, the distance to the view point is decreased yielding a fully transparently rendered outer wall. The 1D color map is depicted on the far right.

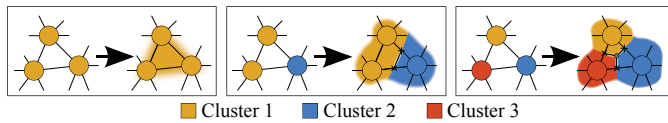


Fig. 7. Adaption of the rendering to depict the clustering result.

slice view conveys cross-sectional views of the inner and outer wall. Finally, the surface clustering can be employed for a cluster-based exploration. The framework is depicted in Figure 10.

Distance ribbons. In general, the *WT* could be visualized via color-coding. However, in our framework color-coding is already employed to depict the surface clusters. Dick et al. [13] presented different ways to illustrate distances of inner and outer structures – in their case a bone and an implant. To convey the thickness, we use *distance ribbons*. Similar to slices, which were used by Dick et al., the distance ribbons wrap the inner and outer structure. They are color-coded from dark to bright blue depending on whether the distances are small or high. Additionally, the distance ribbons on the back side of the outer wall are dashed to impart a spatial impression of the surface, recall Figure 10. They support the depiction of *WT* especially in static images.

Global scatterplot. The *global scatterplot* is used to display the *WT* and the *WSS* of the inner wall, which is divided into different surface clusters visually represented by different colors (recall Sect. 4.4). According to their associated surface clusters, the corresponding points in the global scatterplot are colored identically. The global scatterplot provides an overview of the underlying data of the vessel. For the examinations of data in the global scatterplot, a brushing and linking approach is integrated. The user can brush in the global scatterplot which accentuates the region in the global scatterplot as well as the corresponding parts of the inner wall. If he is interested in, e.g., regions with a high *WSS* and medium *WT*, he can brush this specific polygonal region in the global scatterplot and the corresponding region parts are emphasized with a different colormap, see Figure 8. An eraser tool is also provided to deselect parts of the brushed region.

Local scatterplot. Furthermore, a *local scatterplot* is included. Here, only the data that can be seen in the current 3D scene are plotted. This supports the local examination of the vessel. If the medical expert is interested in specific regions, the local scatterplot allows representing the data of the local observation, see Figure 9.

The slice view. For assessing the wall thickness, a 2D slice view is provided. The slice view provides the cross-section of the vessel along the vessel's centerline and the inner and outer wall is depicted, see Figure 10(d). The parts of the inner wall are color-coded according to their cluster representation. We employed a grid to provide quantitative information and the size of a quadratic grid cell is annotated. In the 3D scene, the position of the currently shown cross-section is highlighted with a green frame (see Fig. 10(a)). The frame can be translated along the vessel and the slice view is updated accordingly. The intersections with the current frame and the inner and outer wall are depicted in the 3D scene as well. For an improved differentiation from the distance ribbons, a small cone-shaped glyph is pointing at the slice view frame in the 3D scene.

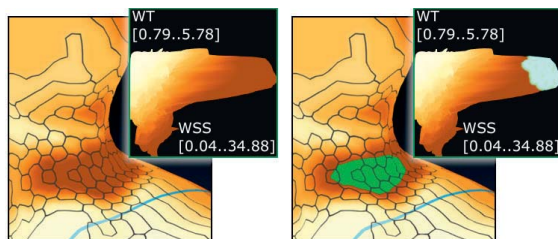


Fig. 8. If the user is interested in regions of high *WSS* and medium *WT*, he can brush a polygonal region in the global scatterplot (inlet) and the region will be emphasized with a different colormap from green to white.

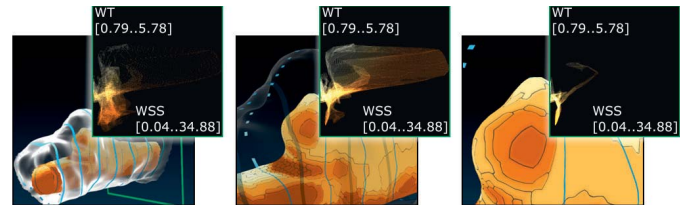


Fig. 9. The local scatterplot (inlet) adapts its appearance according to the specific 3D scene. Therefore, the expert gains insight about the data distribution in the current scene.

Visual exploration of the surface clustering. As described in Section 4.4, different ϵ values are used to obtain different cluster results. Therefore, the user can change the ϵ values to investigate the results. Furthermore, the user can also choose specific clusters. To support medical experts, the clusters are ranked according to their average $\|\vec{r}\|$ value. If the expert selects one cluster, only this cluster is color-coded on the surface, whereas all other surface parts are shaded in gray. If the cluster is currently hidden, it is gradually made visible. For this purpose, an automatic camera path from the current view point to the selected cluster's center is determined. This concept was inspired by [31], where similar camera paths were employed and appreciated by the medical experts.

6 GPU IMPLEMENTATION

In this section, the rendering part of our framework is described in more detail regarding the GPU implementation.

Our surface visualization is divided in a part for the inner wall and a part for the outer wall. The outer wall is conveyed using a Fresnel shading term. The inner wall is color-coded according to the selected parameter space or to the cluster's average parameter. The colorings as well as the corresponding cluster borders are generated in the fragment shader. Therefore, the different cases which may occur will be tested in the geometry shader (recall also Fig. 7). If two vertices have the same cluster ID but not the third vertex, the two vertices are assigned to -1 and the third vertex is assigned to 1. These values were interpolated on the triangle in the fragment shader and therefore the fragment is assigned to a gray value at the zero crossing. This ensures a gray cluster border in the triangle. If all vertices correspond to different surface clusters, every vertex is assigned to the unit vector $(1, 0, 0)$, $(0, 1, 0)$, $(0, 0, 1)$. The cluster border consists of three lines connecting the triangle's edge mid points to the triangle's barycenter.

For the illustration of the scatterplots and the slice view, the extension `EXT_SHADER_IMAGE_LOAD_STORE` is used. This extension allows drawing on specific coordinates on an image. Both scatterplots are initialized as images. The global scatterplot is drawn in an extra shader. Here, all *WSS* and *WT* data are available. These values are scaled according to the image size and plotted on the global scatterplot. The local scatterplot is generated in the fragment shader of the surface visualization. Hence, only fragments are drawn which can be seen in the 3D scene. Thus, the local scatterplot only depends on the fragments of the current 3D scene. The corresponding fragments inherit *WSS* and *WT* information. Thus, every fragment stores its *WSS* and *WT* in the image of the local scatterplot.

The slice view is also generated in an additional shader as slab rendering. A global variable is used to specify the position of the slice view. The shader has also vertex position information. The vertex position will be sent to the fragment shader independently of its visibility in the current view. The fragment shader tests if the 3D coordinates are in the range of the position of the slice view. In this case, the position is drawn on the image of the slice view.

The camera path is determined by using the center of each cluster. With the center's normal, the viewing direction's destination position is determined. Then, a path is extracted from the current viewing position to the end point. Furthermore, the center's normal is employed for a smooth change of the current viewing direction.

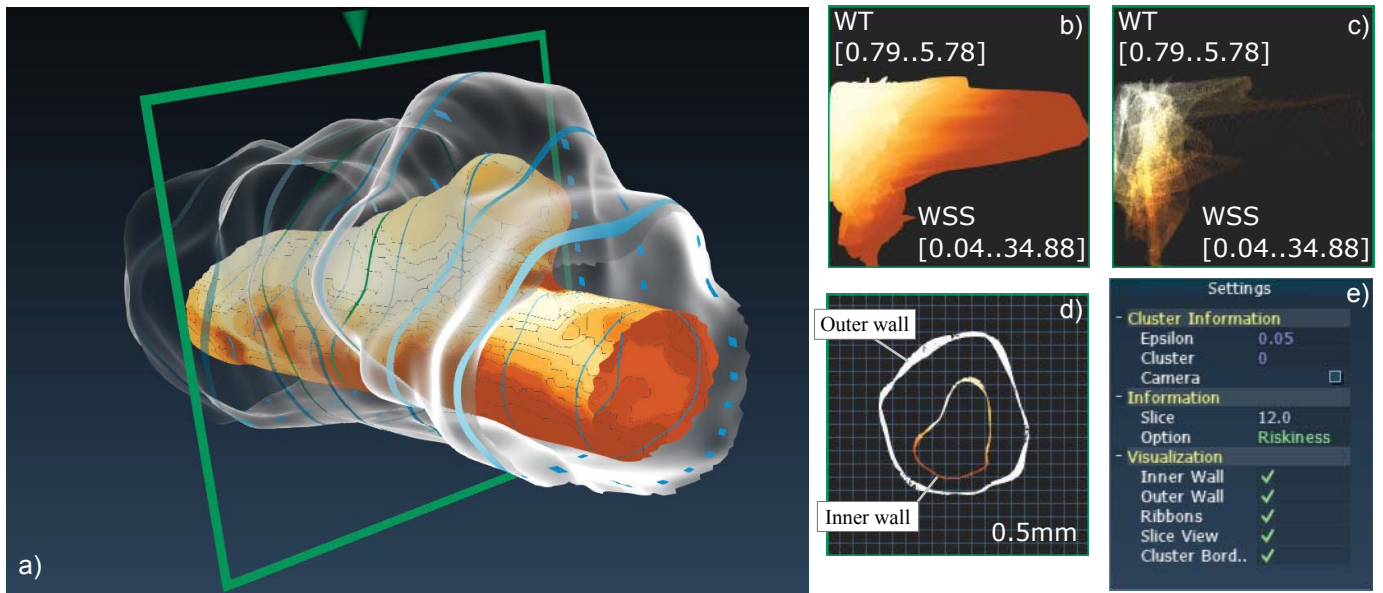


Fig. 10. Presentation of our framework for the exploration of aneurysm wall thickness and wall shear stress. The main area (a), holds the visualization of the inner and the outer wall as well as distance ribbons. On the top right, the global scatterplot (b) and the local scatterplot (c) are depicted. The slice view (d) depicts the vessel wall's cross section. Its position is marked with the green rectangle in (a). Interactive brushing and linking is carried out in the global scatterplot and parameter choices can be set in the user panel (e).

7 EVALUATION

For an evaluation of our combined visualization of *WT* and *WSS*, we prepared a questionnaire. Eleven subjects (one female, ten male, aged 26-41 years) participated in our user study, comprising two experienced neuroradiologists and nine biomedical engineers familiar with vascular diagnosis. The user study began with a short demonstration of the framework and a description of different viewing techniques. Afterwards, each facility was explained in more detail and the users were encouraged to explore the scene on their own in order to answer the questions. They had to try each exploration technique as well as to identify the most suspicious aneurysm parts. We noted the spoken comments of the participants. We used cerebral aneurysms as special application area.

7.1 Questionnaire

For all questions, pre-defined choices were provided to make the results comparable. Besides simple “yes” or “no” and multiple choice questions, a Likert-type scale [27] was employed to rate the suitability of selected techniques. That means, the user can select between -, 0, +, ++. The questionnaire comprises the following aspects.

General aspects. First, we asked for the subject's opinion about the importance of the *WT* for the evaluation of cerebral aneurysms in general. They should also state if they would use our framework. Then, we requested which of the techniques (general exploration of color-coded surface view of inner wall, exploration via clustering, exploration via brushing and linking) is best suited for assessing *WT*. Hence, we were interested in the favorite exploration technique. Finally, the subject should rate the provided distance ribbons, the shaded outer wall, and the slice view regarding their ability to depict the *WT*. We declared the last techniques as supplemental techniques.

Brushing and linking. The second aspect aims at the suitability of the scatterplot-based exploration and the brushing and linking facilities. The users rated the ability to detect critical regions via brushing and linking. Second, they rated the possibility to brush their own parameter combinations, e.g., regions with low *WSS* and low *WT*. Furthermore, they chose how well the distribution of *WSS* and *WT* can be extracted from the global and the local scatterplot.

Clustering. For the presented clustering view, the users should rate if the color-coded clusters are appropriate to identify spatially connected regions with increased $||\vec{r}||$. They could choose the Likert score “- -”

if they didn't like the clusters at all but preferred a direct color-coding of parameters on the inner wall surface. Also, they should rate if the color-coding is well suited to separate regions with high risk from regions with low risk. Next, the subjects rated the ϵ -based exploration of the clustering results. Finally, they evaluated the selection of single clusters to detect dangerous regions. Furthermore, they should assess if various datasets could be compared based on the clustering, i.e., small and many regions indicate a more heterogeneous distribution of *WT* and *WSS*.

Navigation and general remarks. Two questions are related to the navigation. First, the complexity of the necessary navigation to inspect and explore the whole scene was requested. Second, the suitability of the automatic camera path animation had to be rated. Finally, we asked for additional remarks or possible extensions for the presented framework.

7.2 Results

For the interpretation of our pre-defined Likert score categories, we provide the mode value m , i.e., the most frequent answer, and number P of participants who chose “+” or “++”. All users assigned a high importance of wall thickness evaluation for treatment planning of cerebral aneurysms ($m = “++”$; $P = 11/11$) and would employ the presented framework. When choosing their favorite facility to explore the parameters *WT* and *WSS* between color-coded surface visualization, cluster exploration and brushing and linking, the 11 participants chose the brushing and linking (6 users including the medical experts) and the color-coded surface visualization (5 users), see also Figure 11(a). Brushing and linking was chosen due to the direct visual feedback, i.e., the interactive highlighting of surface parts corresponding to the brushed region in the scatter plot. When rating the supporting visualization techniques, the slice view was ranked best with $m = “+”/“++”$ and $P = 10/11$ (see Fig. 11(b)). All users attested an easy navigation ($m = “++”$ $P = 11/11$ for the usability of navigation and the automatic camera paths), since all of them could easily explore the scene in an intuitive way.

The exploration via brushing and linking was substantial for evaluating the 3D aneurysm model and the users most often rated it with $m = “++”$ ($P = 10/11$). They also rated the possibility to detect own parameter combinations via brushing and linking with $m = “++”$ ($P = 9/11$), see Figure 11(c). Especially the medical experts

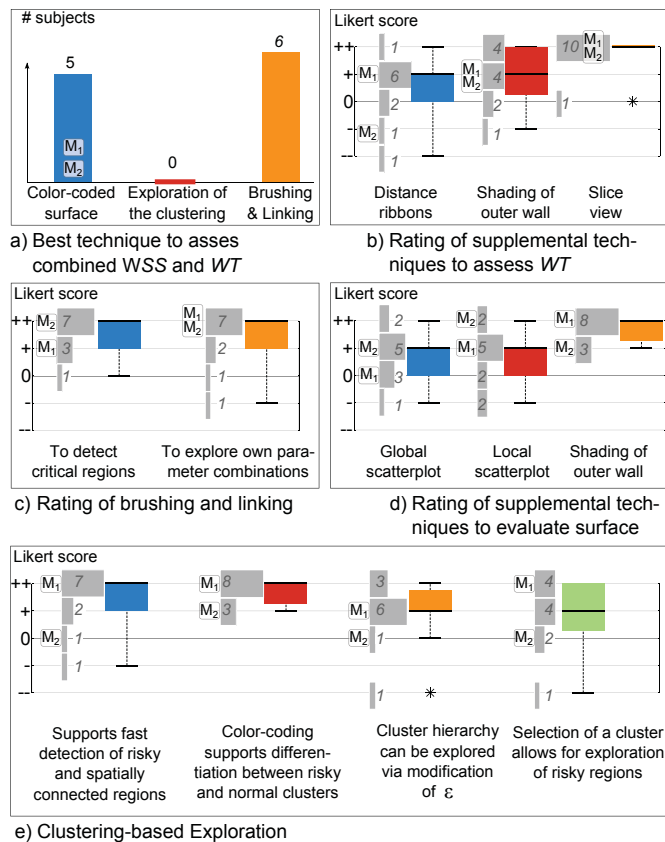


Fig. 11. Selected results of our user study. The box-whisker-plots depict the lower q_1 (25%) and upper q_3 (75%) quartile as well as the median, min and max value. Histograms depict the complete ranking, M_1 and M_2 represent the answers of the medical experts. The extreme values are considered to be outliers (*) if they are at least two interquartile ranges below q_1 , or at least two interquartile ranges above q_3 .

pointed out that a ground truth for the most dangerous parameter combination is still missing. Although they agreed with the pre-defined combination of WT and WSS as riskiness \vec{r} , they stated that for some aneurysm characteristics (e.g., monitoring during longitudinal studies) a modified parameter combination is needed for exploration. Compared to the brushing and linking facility, not all users appreciated the exploration based on the global and local scatterplot ($m = "+"$; $P = 7/11$ for both). They named the missing spatial information as shortcoming of the scatterplot-based exploration. The users liked the adaptive fading of the outer wall visualization very much ($m = "++"$; $P = 11/11$), see Figure 11(d). Hence, the users were not asked to compare the techniques, but rather to rate each of them individually.

The clustering-based exploration enabled the fast detection of dangerous, spatially connected regions ($m = "++"$; $P = 9/11$) and the color-coding favored a fast separation into normal regions of the inner wall and regions with high riskiness ($m = "++"$; $P = 11/11$). Hence, a variation between usefulness of the selection of individual clusters ($m = "+"$ /"++" and $P = 8/11$) and the exploration of the clustering's hierarchy by varying ϵ ($m = "+"$ and $P = 9/11$) could be seen, since one participant did not want to use the automatic division into clusters (see also Fig. 11(e)). Interestingly, the clinical experts approved the clustering-based exploration. When asked for a Likert score regarding the possibility of comparison different datasets based on the clustering results, the users answered with $m = "+"$ /"++" and $P = 11/11$.

8 DISCUSSION

All users quickly adapted to the presented framework. The informal evaluation and especially the discussion with the medical experts indicated the importance of WT for aneurysm evaluation. The participants

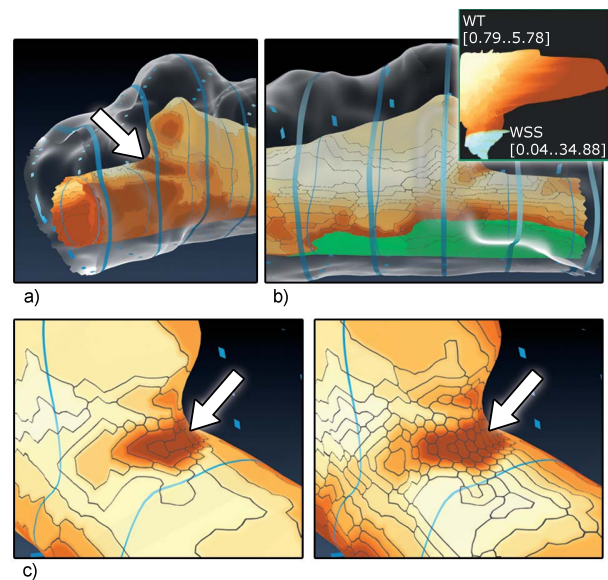


Fig. 12. Selected aspects during the user exploration. In (a), the salient region is shown. In (b), an important finding is visualized. During the brushing of a user-defined parameter combination, the highlighted regions at the bottom of the parent vessel were identified. In (c), different cluster results (based on varying ϵ values) still reveal the salient region.

also stated that wall morphology and thickness are the most important missing information for rupture risk (due to the missing in vivo imaging technique) based on their clinical experience. In general, the users would definitely employ our framework for simultaneous evaluation of WSS and WT . During evaluation, two main techniques were discussed in depth: the brushing and linking and the clustering. These aspects will be described in the following. Next, minor improvements and suggestions are listed. Finally, we discuss general aspects regarding the image acquisition and provide a short discussion for another application area to demonstrate the practicalness of our method.

Brushing and linking. Most users chose the brushing and linking-based exploration since they could also highlight own parameter combinations (see Fig. 11(a)). Hence, the clinical experts referenced the missing gold standard of rupture risk parameters, recall Section 3. They pointed out that the brushing and linking and thus the highlighting of certain surface parts support the communication and sharing of knowledge. During exploration, all participants explored the regions with high WSS and low WT at the most salient surface part, see Figure 12(a). Pointed out by one user, an interesting feature was detected at the bottom of the aneurysm parent vessel, see Figure 12(b). Hence, a thin wall and low WSS values were brushed yielding the highlighted surface parts. In clinical practice, these regions are important to completely characterize the relationship between vessel topology and hemodynamic behavior. The clinicians stated that also areas with wall thinning (and thus increased rupture risk) can be a consequence of reduced blood flow and lower but oscillating WSS values (recall Sect. 3). One medical expert asked for an additional feature: a reversed brushing and linking concept. That means, a brushing in the dataspace (on the inner vessel wall surface) causes a linked highlighting in the attribute space (the local and global scatterplots). Although this relationship can be explored via cluster selection (selected cluster is highlighted on the surface, as well as its parameter values in the scatterplots) a brushing and linking concept in this domain seems to be interesting. As a first alternative, we included a 2D transfer function to map the combination of WT and WSS in our framework, see Figure 13. Therefore, the user can choose between the 1D color map (for WSS , WT or $||\vec{r}||$, see Fig. 6) and the novel 2D color map.

Clustering-based exploration. The pre-extracted clusters were discussed controversially. On the one hand, many users (8 of 11) liked the clustering as well as the ϵ -based exploration of the hierarchical clus-

tering structure (recall Sect. 5.3). That means, with smaller ε values, the region merging process is stopped earlier. Therefore, more clusters at heterogeneous regions, i.e., regions with strong variations for the parameter values, will remain and not be merged, see Figure 12(c). The users didn't request a clustering based on different parameter combinations but instead combined it with the brushing and linking technique for this purpose. The user who did not like the clustering, explained that he did not get any benefit from the clustering. Hence, we suggest to use the direct color-coding of one of the parameters WT , WSS or $||\vec{r}'||$. We also want to clarify that our clustering visualization is purely supplemental. At the moment, it is not aiming at any automatic parameter extraction or classification.

Minor aspects. After the evaluation, minor improvements were requested by the users. For example, the inclusion of measurement tools to approximate the WT was suggested. Also, they asked for additional quantitative information about the cluster's average parameter values. Furthermore, a user suggested distance ribbons with varying width adapted to WT . This would lead to very broad ribbons in areas of thicker walls and induce occlusion problems. Finally, we have to consider a possible improvement of our snake-based segmentation. Although it works fine for our prepared aneurysm, more approaches, e.g., level sets, exist. We adapted the level set method as well, but empirically achieved worse results compared to the snake-based segmentation. In [5], a comparison of different IVUS 2D and 3D segmentation techniques is provided. Also, a co-registration with biplane angiography image data is possible. Due to the presented setup, i.e., the parent vessel was fixated along the z-axis, this step was not necessary.

Outlook. The presented framework can be extended to various application areas comprising aneurysms in general as well as inner and outer vessel walls. Furthermore, the work can be adapted to surfaces enclosing a focus structure. Therefore, we examined a study of functional MRI datasets of the left ventricle, i.e., the heart muscle also called myocardium, from patients that suffered from a heart attack. Although contrast-enhanced datasets are acquired to locate the infarction scar and the myocardial viability, the functional MRI data holds valuable information about the heart muscle's contractility. Typically, the infarction causes a reduced ability of muscle tension. Hence, the clinical expert does not only want to locate the infarction scar and necrotic tissue, but to assess the influence of the infarction for the myocardial function as well. For clinical evaluation, the heart cycle is analyzed from the time of end diastole (the myocardium is fully relaxed) until end systole (maximum contraction is achieved).

The adaption of our framework is demonstrated in Figure 14. It is related to the CoViCAD approach [38], where the left ventricular wall is mapped to a volumetric bull's eye plot with additional anatomical context. Hence, the wall thickness is mapped to the height of a cylinder or depicted as region of interest mapped on a rectangle. The left ventricle consisting of epicardium and endocardium, i.e., the myocardium, is visualized with the outer wall shading and the color-coded surface view. The myocardial contractility is extracted as wall thickening. Therefore, the wall thickness at end diastole and end systole is approximated. The wall thickening is then calculated as increased wall thickness at end systole and color-coded.

This whole work was accomplished as part of a large research project where the refinement and miniaturization of catheters is a ma-

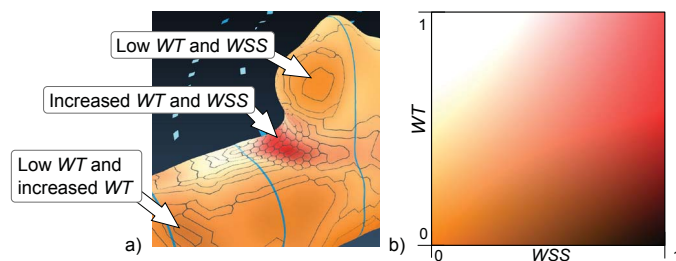


Fig. 13. The 2D color map for the combined depiction of WT and WSS .

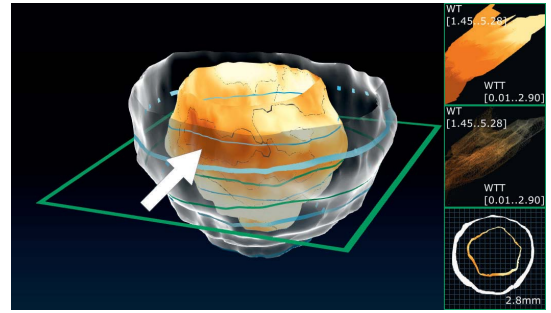


Fig. 14. Adaption of our framework to assess myocardial infarctions. Hence, the myocardial contractility is analyzed to detect regions on the myocardial surface with reduced wall thickening from end diastole to end systole. Parts of the myocardium are characterized by reduced wall thickening due to a heart attack (see arrow).

ior project goal. Thus, the measurement of vessel wall properties in the cerebral arteries is intended in the future to provide real clinical data.

9 CONCLUSION AND FUTURE WORK

In this paper, we presented a framework for the simultaneous exploration of hemodynamic information, i.e., the WSS , and the wall thickness WT . Our work is a first step towards the integration of the vessel wall morphology in the image-based evaluation of aneurysms and similar vascular diseases. More generally, the presented visualization and exploration concepts can be applied to the inner and outer vessel wall and additional information, like the extracted WSS . Our framework depicts the outer and inner wall and avoids occlusions. Color-coding is employed on the inner vessel wall surface to depict (cluster-based) parameter values. Furthermore, the exploration is improved with a global and a local scatterplot (including brushing and linking facilities) as well as a slice view and the clustering-based exploration. The presented framework is the first framework that provides a combined visualization of wall thickness and hemodynamic information for a dissected cerebral aneurysm. It was developed for the medical researcher to simultaneously examine WSS and WT .

Our pipeline covers IVUS imaging of vessel walls – a scenario that could be applied to cerebral aneurysms in near future. Due to the novelty of this research area, many extensions are possible. An example is the improved CFD simulation that accounts for the vessel wall thickness and its elastographic properties. Also, the influence of different image acquisition techniques, like optical coherence tomography (OCT) [22], will be examined in the near future. For instance, improved image modalities, i.e., higher resolution image datasets, will not only provide the vessel wall thickness but also the vessel wall's pathologic parts, e.g., plaque burden, calcified parts of the vessel wall as well as its elastographic properties. Recently, OCT yielded promising results in intravascular coronary imaging and a better image resolution than IVUS [23]. However, similar to IVUS, no admission for the in vivo imaging of the cerebral vascular system is available yet. Finally, we are working on the inclusion of streamline visualization to reveal additional information like hemodynamic vortices or increased inflow jets.

ACKNOWLEDGMENTS

The work was partly funded by the German Ministry of Education and Research (BMBF) within the *STIMULATE* project (grant no. 03FO16101A). We thank Uta Preim (Municipal Hospital Magdeburg, Germany) and Oliver Beuing (University Hospital Magdeburg, Germany) for their medical input. The simulated flow data was provided by Philipp Berg and Gabor Janiga (Institute of Fluid Mechanics and Thermodynamics at the University of Magdeburg, Germany).

REFERENCES

- [1] R. Adams and L. Bischof. Seeded Region Growing. *IEEE Transactions on Pattern Analysis and Machine Intelligence*, 16(6):641–647, 1994.
- [2] M. Attene, S. Katz, M. Mortara, G. Patané, M. Spagnuolo, and A. Tal. Mesh Segmentation – A Comparative Study. In *Proc. of IEEE Shape Modeling and Applications*, pages 7–18, 2006.
- [3] A. Baer, R. Gasteiger, D. Cunningham, and B. Preim. Perceptual Evaluation of Ghosted View Techniques for the Exploration of Vascular Structures and Embedded Flow. *Computer Graphics Forum*, 30(3):811–820, 2011.
- [4] L. Baldacci, M. Golfarelli, A. Lumini, and S. Rizzi. Clustering Techniques for Protein Surfaces. *Pattern Recognition*, 39(12):2370–82, 2006.
- [5] S. Balocco, C. Gatta, F. Ciompi, A. Wahle, P. Radeva, S. Carlier, G. Unal, E. Sanidas, J. Mauri, X. Carrillo, T. Kovarnik, C.-W. Wang, H.-C. Chen, T. P. Exarchos, D. I. Fotiadis, F. Destrempes, G. Cloutier, O. Pujol, M. Alberti, E. G. Mendizabal-Ruiz, M. Rivera, T. Aksoy, R. W. Downe, and I. A. Kakadiaris. Standardized Evaluation Methodology and Reference Database for Evaluating IVUS Image Segmentation. *Computerized Medical Imaging and Graphics*, 38(2):70–90, 2014.
- [6] D. Balzani, D. Böse, D. Brands, R. Erbel, A. Klawonn, O. Rheinbach, and J. Schröder. Parallel Simulation of Patient-Specific Atherosclerotic Arteries for the Enhancement of Intravascular Ultrasound Diagnostics. *Engineering Computations*, 29(8):888–906, 2012.
- [7] S. Bruckner, S. Grimm, A. Kanitsar, and E. Gröller. Illustrative Context-Preserving Volume Rendering. *IEEE Transactions on Visualization and Computer Graphics*, 12:1559–1569, 2006.
- [8] J. R. Cebral, M. A. Castro, S. Appanaboyina, C. M. Putman, D. Milan, and A. F. Frangi. Efficient Pipeline for Image-Based Patient-Specific Analysis of Cerebral Aneurysm Hemodynamics: Technique and Sensitivity. *IEEE Transactions on Medical Imaging*, 24(4):457–467, 2005.
- [9] J. R. Cebral, F. Mut, J. Weir, and C. Putman. Association of Hemodynamic Characteristics and Cerebral Aneurysm Rupture. *American Journal of Neuroradiology*, 32(2):264–70, 2011.
- [10] J. R. Cebral, F. Mut, J. Weir, and C. Putman. Quantitative Characterization of the Hemodynamic Environment in ruptured and unruptured Brain Aneurysms. *American Journal of Neuroradiology*, 32(1):145–51, 2011.
- [11] J. R. Cebral, M. Sheridan, and C. M. Putman. Hemodynamics and Bleb Formation in Intracranial Aneurysms. *American Journal of Neuroradiology*, 31(2):304–310, 2010.
- [12] T. Crawford. Some Observations on the Pathogenesis and Natural History of Intracranial Aneurysms. *Journal of Neurology, Neurosurgery, and Psychiatry*, 22(4):259–266, 1959.
- [13] C. Dick, R. Burgkart, and R. Westermann. Distance Visualization for Interactive 3D Implant Planning. *IEEE Transactions on Visualization and Computer Graphics*, 17(12):2173–82, 2011.
- [14] H. Doleisch, M. Gasser, and H. Hauser. Interactive Feature Specification for Focus+Context Visualization of Complex Simulation Data. In *Proc. of Symposium on the Data Visualization*, pages 239–248, 2003.
- [15] J. Frösen, A. Piippo, A. Paetau, M. Kangasniemi, M. Niemelä, J. Hernesniemi, and J. Jääskeläinen. Remodeling of Saccular Cerebral Artery Aneurysm Wall Is Associated with Rupture: Histological Analysis of 24 Unruptured and 42 Ruptured Cases. *Stroke*, 35(10):2287–2293, 2004.
- [16] R. Gasteiger, D. J. Lehmann, R. van Pelt, G. Janiga, O. Beuing, A. Vilanova, H. Theisel, and B. Preim. Automatic Detection and Visualization of Qualitative Hemodynamic Characteristics in Cerebral Aneurysms. *IEEE Transactions on Visualization and Computer Graphics*, 18(12):2178–2187, 2012.
- [17] R. Gasteiger, M. Neugebauer, C. Kubisch, and B. Preim. Adapted Surface Visualization of Cerebral Aneurysms with Embedded Blood Flow Information. In *Proc. of Visual Computing for Biology and Medicine*, pages 25–32, 2010.
- [18] D. Gil, P. Radeva, J. Saludes, and J. Mauri. Automatic Segmentation of Artery Wall in Coronary IVUS Images: a Probabilistic Approach. In *Proc. of Computers in Cardiology*, pages 687–690, 2000.
- [19] S. Gläser, S. Oeltze, A. Hennemuth, C. Kubisch, A. Mahnken, S. Wilhelmssen, and B. Preim. Automatic Transfer Function Specification for Visual Emphasis of Coronary Artery Plaque. *Computer Graphics Forum*, 29(1):191–201, 2010.
- [20] F. V. Higuera, N. Sauber, B. Tomandl, C. Nimsky, G. Greiner, and P. Hasltreiter. Automatic Adjustment of Bidimensional Transfer Functions for Direct Volume Visualization of Intracranial Aneurysms. In *Proc. of SPIE Medical Imaging*, pages 275–284, 2004.
- [21] V. Interrante, H. Fuchs, and S. Pizer. Enhancing Transparent Skin Surfaces with Ridge and Valley Lines. In *Proc. of IEEE Visualization*, pages 52–59, 1995.
- [22] F. Ishida, H. Ogawa, T. Simizu, T. Kojima, and W. Taki. Visualizing the Dynamics of Cerebral Aneurysms with Four-Dimensional Computed Tomographic Angiography. *Neurosurgery*, 57(3):460–471, 2005.
- [23] I.-K. Jang, B. E. Bouma, D.-H. Kang, S.-J. Park, S.-W. Park, K.-B. Seung, K.-B. Choi, M. Shishkov, K. Schlendorf, E. Pomerantsev, et al. Visualization of Coronary Atherosclerotic Plaques in Patients Using Optical Coherence Tomography: Comparison with Intravascular Ultrasound. *Journal of the American College of Cardiology*, 39(4):604–609, 2002.
- [24] L. M. Kadasi, W. Dent, and A. M. Malek. Cerebral Aneurysm Wall Thickness Analysis Using Intraoperative Microscopy: Effect of Size and Gender on thin Translucent Regions. *Journal of Neurointerventional Surgery*, 5(3):201–206, 2013.
- [25] M. Kass, A. Witkin, and D. Terzopoulos. Snakes: Active contour models. *International Journal of Computer Vision*, 1(4):321–331, 1988.
- [26] K. Lawonn, R. Gasteiger, and B. Preim. Adaptive Surface Visualization of Vessels with Animated Blood Flow. *Computer Graphics Forum*, in print, doi: 10.1111/cgf.12355, 2014.
- [27] R. Likert. A Technique for the Measurement of Attitudes. *Archives of Psychology*, 22(140):55, 1932.
- [28] M. Markl, A. Frydrychowicz, S. Kozerke, M. Hope, and O. Wieben. 4D Flow MRI. *Journal of Magnetic Resonance Imaging*, 36(5):1015–1036, 2012.
- [29] D. Meyers, S. Skinner, and K. Sloan. Surfaces from Contours. *ACM Transactions On Graphics*, 11(3):228–258, 1992.
- [30] M. Neugebauer, R. Gasteiger, O. Beuing, V. Diehl, M. Skalej, and B. Preim. Map Displays for the Analysis of Scalar Data on Cerebral Aneurysm Surfaces. *Computer Graphics Forum*, 28(3):895–902, 2009.
- [31] M. Neugebauer, K. Lawonn, O. Beuing, P. Berg, G. Janiga, and B. Preim. AmniVis - A System for Qualitative Exploration of Near-Wall Hemodynamics in Cerebral Aneurysms. *Computer Graphics Forum*, 32(3):251–260, 2013.
- [32] M. L. Raghavan, J. Kratzberg, E. M. C. de Tolosa, M. M. Hanaoka, P. Walker, and E. S. da Silva. Regional Distribution of Wall Thickness and Failure Properties of Human Abdominal Aortic Aneurysm. *Journal of Biomechanics*, 39(16):3010 – 16, 2006.
- [33] G. Sakas, L. Schreyer, and M. Grimm. Preprocessing and volume rendering of 3d ultrasonic data. *IEEE Computer Graphics and Applications*, 15(4):47–54, 1995.
- [34] C. Schlick. A Customizable Reflectance Model for Everyday Rendering. In *Proc. of Eurographics Workshop on Rendering*, pages 73–83, 1993.
- [35] J. Schöberl. Netgen: An Advancing Front 2D/3D-Mesh Generator based on Abstract Rules. *Computing and Visualization in Science 1*, pages 41–52, 1997.
- [36] A. Shamir. A Survey on Mesh Segmentation Techniques. *Computer Graphics Forum*, 27(6):1539–1556, 2008.
- [37] P. C. Tang, M. A. Coady, C. Lovoulos, A. Dardik, M. Aslan, J. A. Elefteriades, and G. Tellides. Hyperplastic Cellular Remodeling of the Media in Ascending Thoracic Aortic Aneurysms. *Circulation*, 112(8):1098–1105, 2005.
- [38] M. Termeer, J. O. Bescs, M. Breeuwer, A. Vilanova, F. Gerritsen, and E. Gröller. CoViCAD: Comprehensive Visualization of Coronary Artery Disease. *IEEE Transactions on Visualization and Computer Graphics*, 13(6):1632–1639, 2007.
- [39] V. D. Tsakanikas, L. K. Maichalis, D. I. Fotiadis, K. K. Naka, and C. V. Bourantas. *Intravascular Imaging: Current Applications and Research Developments*. IGI Global, 2012.
- [40] P. M. A. van Ooijen, R. J. M. van Geuns, B. J. W. M. Rensing, A. H. H. Bongaerts, P. J. de Feyter, and M. Oudkerk. Noninvasive Coronary Imaging Using Electron Beam CT: Surface Rendering Versus Volume Rendering. *American Journal of Roentgenology*, 180(1):223–226, 2003.
- [41] I. Viola. *Importance-Driven Expressive Visualization*. PhD thesis, Institute of Computer Graphics and Algorithms, Vienna University of Technology, 2005.
- [42] M. J. Wermer, I. C. van der Schaaf, A. Algra, and G. J. Rinkel. Risk of Rupture of Unruptured Intracranial Aneurysms in Relation to Patient and Aneurysm Characteristics An Updated Meta-Analysis. *Stroke*, 38(4):1404–1410, 2007.
- [43] D. O. Wiebers. Unruptured Intracranial Aneurysms: Natural History, Clinical Outcome, and Risks of Surgical and Endovascular Treatment. *The Lancet*, 362(9378):103–110, 2003.